RSC Advances

ROYAL SOCIETY OF CHEMISTRY

www.rsc.org/advances

Optimized design of multi-shell ZnO/TiO_2/ZnSe nanowires decorated with Ag nanoparticles for photocatalytic applications

Li Zhan[a], Jialun He[a], Weiping Wang[a], Xuanli Zheng[a], Yiyan Cao[a], Jun Yin[a], Lijing Kong[a]*, Qiang Zou[b], Waseem Ahmed Bhutto [a], Xiaohong Chen[a], Shuping Li[a], Zhiming Wu[ab]* and Junyong Kang[a]

a. Fujian Provincial Key Laboratory of Semiconductors and Applications, Collaborative Innovation Center for Optoelectronic Semiconductors and Efficient Devices, Department of Physics, Xiamen University, Xiamen 361005, P. R. China.

b. Center for Nanophase Materials Sciences, Oak Ridge National Laboratory, Oak Ridge, Tennessee, 37831, USA

Corresponding Authors:

Fax: +86-592-2181366; Tel: +86-5922180858

E-mail: zmwu@xmu.edu.cn; lijing-k@xmu.edu.cn

Abstract

Composite nanomaterials consisting of semiconductor sensitizers and noble metal nanoparticles (NPs) exhibit great potential for high-efficiency photocatalytic applications. However, the differences in structure can significantly affect the light utilization efficiency and photocatalytic performance. In this study, we report the structural design of multi-shell coaxial nanowires (NWs) for their applications in photocatalytic degradation. Two types of multi-shell coaxial NWs, namely, ZnO/TiO_2/ZnSe/Ag(NPs) and ZnO/TiO_2/Ag(NPs)/ZnSe NWs, were successfully fabricated. Experimental and theoretical results revealed that surface structures and the position of Ag NPs in coaxial NWs significantly influenced the intensity of localized surface plasmon resonance, light absorption, and photocatalytic performance. The photocatalytic activity of the ZnO/TiO_2/Ag(NPs)/ZnSe NWs was significantly enhanced under UV and visible light irradiation compared with that of the ZnO/TiO_2/ZnSe/Ag(NPs) NWs. The improved performance was explained by electron transfer models combined with band structure alignment. Furthermore, an optimal NW structure was proposed on the basis of the analysis of photocatalytic mechanisms. This study provides guidance to the design of composite materials for high-efficiency photocatalytic applications.

Key words:

Photocatalysis degradation; Multi-shell nanowires; Localized surface plasmon resonance; Structural design

1. Introduction

Photocatalytic degradation of organic pollutants has become a hot research topic because of the growing awareness of environmental protection and the shortage of clean water sources[1-4]. Traditional treatment methods, such as adsorption, coagulation, and membrane separation, suffer from incomplete elimination of pollutants or generation of secondary pollutants. Currently, advanced oxidation processes (AOPs) is regarded as an effective way to degrade organic contaminants, and heterogeneous photocatalysis by using semiconductor catalysts, such as TiO_2, ZnO, Fe_2O_3, CdS, GaP, and ZnS, has been widely investigated [1-3]. Among the semiconductor catalysts, titanium dioxide (TiO_2) has received the greatest interest because of its low cost, high photocatalytic activity, and stability [4, 5]. However, TiO_2 has a relatively wide bandgap and cannot efficiently absorb sunlight in visible regions, resulting in its low efficiency. Several strategies, such as doping with metals (Cr and V) or non-metals (NO_x and N) and the synthesis of composite photocatalysts, have been proposed to enhance light absorption [6-10]. Among these techniques, the synthesis of composite photocatalysts is most preferable because of their effective photoresponse. Hence, semiconductors with a narrow bandgap, such as ZnSe or CdSe nanocrystals, are often used as sensitizers coated on the outside of NWs [11-13].

TiO_2-based nanostructures decorated with noble metal NPs are also intensively investigated [14, 15]. On the one hand, the Schottky junction that

forms at the interface of metal/semiconductors effectively suppresses the recombination of electrons and holes, thereby enhancing photocatalytic effects. On the other hand, noble metal NPs can induce localized surface plasmon resonance (LSPR), which enhances the visible light absorption. Among reported literatures [16-19], Ag NPs have been extensively adopted as decorated materials because of their relatively low cost, high catalytic efficiency, and strong LSPR effect in the visible light range. For instance, Awazu et al. proposed a plasmonic photocatalyst consisting of Ag NPs embedded in TiO_2 and achieved an enhancement of photocatalytic activity by a factor of 7 [19]. It is quite reasonable to believe that the combination of semiconductor sensitization and noble metal NPs decoration could yield further enhancement of photocatalytic performance. Ren et al. synthesized sandwiched ZnO@Ag@Cu_2O nanorods and observed enhanced photocatalytic performance in the visible light range [20]. Zhang et al. reported composite ZnO/Ag/CdS NWs, which exhibited significantly enhanced photocatalytic properties [21]. Such enhanced behaviors are usually attributed to the strengthened near field induced by the LSPR effect. Nevertheless, the surface electromagnetic field of noble metals is easily influenced by adjacent dielectric materials in composite structures. Moreover, differences in structure affect the coupling of LSPR-enhanced fields with semiconductors, light utilization efficiency, and photocatalytic mechanism. An immoderate structure can deteriorate the LSPR effect and photocatalytic performance. Thus far, only few studies have reported

optimizing the design of combined semiconductor sensitizers and noble metal NPs for photocatalytic applications.

In this work, two types of multi-shell coaxial NWs, namely, ZnO/TiO_2/ZnSe/Ag(NPs) and ZnO/TiO_2/Ag(NPs)/ZnSe NWs, were successfully fabricated, and the dependence of photocatalytic performance on structures was investigated. Scanning electron microscopy (SEM), transmission electron microscopy (TEM), X-ray diffraction (XRD), transmission analysis, and finite difference time domain (FDTD) simulation were performed to investigate the morphologies, structures, optical properties, and near-field distribution of coaxial NWs. Enhanced photocatalytic activities in both structures were achieved in UV and visible light ranges. A significant structure dependence of the enhancement effect was also observed. Electron transfer models combined with band structure alignment were used to explain their differences of photocatalytic activities in terms of photocatalytic mechanism. Finally, an optimal structure of multi-shell ZnO/TiO_2/ZnSe NWs decorated with Ag NPs for photocatalytic applications was proposed.

2. Experimental section

2.1 Materials fabrication

The detailed fabrication process of nanostructures is illustrated in Fig. 1. ZnO NWs were synthesized by CVD method. High-purity metallic Zn powder (99.999%, 0.3 g) was used as the source material and placed at the central

heating zone. An Al-doped zinc oxide (AZO) substrate was placed downstream of the Zn source. The system was evacuated to a pressure of 1.0×10^{-2} Pa, and 50 sccm N_2 flow was introduced into the tube prior to heating. Then, the tube was heated to 500 °C at a rate of 20 °C min^{-1}. Then, O_2 with a flow rate of 4 sccm was passed into the tube when the temperature reached 500 °C. The reaction was maintained for 30 min.

The TiO_2 and ZnSe shell layers were deposited via radio-frequency magnetron sputtering in an Ar atmosphere while the Ag layer was fabricated via the direct current magnetron sputtering method. TiO_2 (99.99%), ZnSe (99.99%), and Ag (99.999%) were used as their sources, respectively. The vacuum chamber was evacuated down to 4×10^{-4} Pa prior to the deposition. Working pressure was maintained at 0.8 Pa, and sputtering powers were set to 300, 80, and 60 W, respectively. The growth times for TiO_2, ZnSe, and Ag were 20 min, 2 min, and 10 s, respectively. The samples were annealed at 450 °C for 5 h and 350 °C for 2 h under N_2 ambient atmosphere after the TiO_2 and ZnSe deposition. Thermal treatment was performed using rapid thermal annealing at 400 °C for 2 min to fabricate the Ag NPs.

2.2 Characterization

The morphologies were characterized using field emission SEM (ZEISS SIGMA). The structures and compositions were analyzed via XRD (Rigaku Ultima IV) and TEM (Tecnai F30 operating at 300 kV). Energy dispersive spectroscopy (EDS) for composition analysis was also performed at a voltage

of 20 kV by using the Tecnai F30. The absorption spectra of the samples were measured using a UV-vis-NIR spectrophotometer (VarianCary, 5000). Raman measurements were performed at room temperature on the Renishaw inVia Raman system with a 532 nm line laser as the excitation source. The intensity of the Raman signal of R6G was considered as the indicator for estimating different samples under UV and visible light irradiation to rapidly obtain effective photocatalytic measurement results. A Xe lamp with a 400 nm cut-off filter at a power 500 W was used as the visible light source during irradiation. A UV lamp made by Philips with a power of 18 W was used as the UV light source. The emission wavelength of the UV lamp ranged from 340 nm to 410 nm. Near-field distributions were simulated at typical incident angles of 90° by using the FDTD method.

3. Results and discussion

The morphologies of bare ZnO NWs and different coaxial NWs were first observed by using SEM. Fig. 2(a) shows the SEM image of ZnO NWs, which exhibited vertical growth and smooth surface. After the deposition of different materials, the coaxial NWs showed a pyramidal shape with a larger diameter and rougher surface compared with the bare ZnO NWs, which indicated the formation of a coaxial structure (Figs. 2(b)-(d)). In our experiment, a 10 nm-thick Ag film was grown and annealed at 400 °C to obtain Ag NPs. As a result, Ag NPs with a diameter of approximately 10-30 nm formed on the

surface (Figs. 2(b) and (c)). The ZnO/TiO_2/Ag/ZnSe NWs (Fig. 2(d)) retained their granular surfaces despite the ZnSe deposition.

Fig. 3 shows the XRD patterns of the ZnO NWs and different composite coaxial NWs. A sharp peak at 34.4° was observed for the bare ZnO NWs,which was indexed to the (002) planes of wurtzite ZnO. Another peak at 31.1° originated from the AZO substrate. Additional characteristic peaks appeared in the XRD patterns after shell growth. The peaks at 25.3° were ascribed to the (101) plane of the anatase phase TiO_2. Interestingly, another distinguished peak at 36.1°, which corresponded to the (101) plane of the rutile phase TiO_2, was observed in the patterns of the ZnO/TiO_2/ZnSe/Ag and ZnO/TiO_2/Ag/ZnSe coaxial NWs. This peak should be attributed to the additional annealing treatment after the growth of ZnSe and Ag. In this sense, the TiO_2 shell comprised the crystal phases of the anatase-rutile mixture, which are highly beneficial for photocatalytic degradation [22-26]. In addition, the peaks at 27.16° and 38.11° could be indexed to the (111) planes of ZnSe and Ag, respectively. In the light of these, the characteristic peaks ideally matched the nominal compositions of the coaxial NWs, demonstrating the successful fabrication of multi-shell coaxial NWs.

To elucidate the structures of the ZnO/TiO_2/ZnSe/Ag and ZnO/TiO_2/Ag/ZnSe coaxial NWs, detailed investigations were conducted by using TEM and EDS. Fig. 4(a) shows the low-magnification TEM image of a ZnO/TiO_2/ZnSe/Ag NW. The ZnO core was fully covered by shell layers, and

small NPs with an average diameter of approximately 20 nm adhered to the surface. This characteristic is in accordance with the SEM result shown in Fig. 2. Fig. 4(b) shows the EDS line-scan profile along the line marked in Fig. 4(a). The distributions of Zn, O, Ti, Se, and Ag elements effectively matched the ZnO/TiO_2/ZnSe/Ag coaxial structure. Fig. 4(c) shows the high-resolution TEM (HRTEM) image of the shell layer. The rightmost image could be ascribed to anatase TiO_2 with [101] growth direction and interplanar spacing of 0.352 nm, whereas the middle layer corresponded to zinc blende ZnSe with [111] growth direction and interplanar spacing of 0.324 nm. Meanwhile, an Ag NP was deposited on the surface, showing a fringe spacing of 0.234 nm.

Similarly, TEM and EDS measurements on ZnO/TiO_2/Ag/ZnSe coaxial NWs were carried out. Figs. 5(a) and (b) show the low-magnification TEM image and EDS line-scan profile, respectively, which confirm a ZnO/TiO_2/Ag/ZnSe coaxial structure. Figs. 5(c) and (d) present the HRTEM images, which exhibits different types of surface structures. In Fig. 5(c), the Ag NP is fully covered by a ZnSe layer and is inlaid between the ZnSe and TiO_2 layers. By contrast, in Fig. 5(d), the Ag NP is partially exposed to air, and a ZnSe quantum dot stands in isolation over the Ag NP. Actually, we also found that some Ag NPs were partially covered by a ZnSe layer, but this layer was still in contact with the TiO_2 layer. The different structures were attributed to the random shrinkage of the thin ZnSe layer during annealing. The differences

in the structures of these NWs could significantly influence their light absorption and photocatalytic activities.

Fig. 6(a) shows the UV-vis absorption spectra of the different samples. The ZnO NWs revealed a sharp band-edge absorption at around 380 nm. The absorption edge almost did not shift after the TiO_2 deposition because of its similar bandgap to ZnO. However, visible light absorption was enhanced because of defect-related absorption [27-30]. The continuous deposition of ZnSe or Ag on the ZnO/TiO_2 NWs further enhanced the light absorptions. The additional ZnSe shell layer on the ZnO/TiO_2/ZnSe NWs only resulted in the stronger absorption at the 400-500 nm region relative to the ZnO/TiO_2 NWs because of the ZnSe band-edge absorption (curve III). Interestingly, the additional Ag NPs led to a significant absorption enhancement over the entire visible region with a peak at ~550 nm (curve IV). This effect indicated the high-efficiency utilization of solar light, which could be attributed to the Ag NPs induced LSPR effect [31]. As we know, the LSPR peak position significantly depends on the size of the metal NPs, that is, a sharp peak is observed for the uniform-sized NPs [32-34]. In our experiment, the size of the Ag NPs exhibited a broad distribution, which resulted in the broadening of the absorption peak. The ultimate NWs, namely, ZnO/TiO_2/ZnSe/Ag and ZnO/TiO_2/Ag/ZnSe coaxial NWs, presented a strong light absorption over the entire visible region because of the collective impact of the ZnSe sensitization and Ag NPs induced LSPR effect. The ZnO/TiO_2/Ag/ZnSe coaxial NWs showed the better absorption performance despite having the same composition

as the other NWs. To further clarify the essence, the near-field distributions of the ZnO/TiO_2/ZnSe/Ag and ZnO/TiO_2/Ag/ZnSe coaxial NWs under visible light irradiation were simulated with the FDTD method. As shown in Figs. 6(b-d), the enhanced local field near the Ag NP could be clearly observed in these three types of structures because of the LSPR effect. Interestingly, the local field in the ZnO/TiO_2/Ag/ZnSe NW obviously indicated the strengthened light absorption shown in Fig. 6(a). The strengthened field can be attributed to the cover of the ZnSe shell layer and, accordingly, to the increase of the induced charges and enhancement of the LSPR effect [20, 21, 35, 36]. Notably, in the case of the ZnO/TiO_2/Ag/ZnSe NWs fully covered by the ZnSe layer (Fig. 6(c)), the strengthened field was fully confined in the ZnSe shell layer, thus indicating high light absorption. By contrast, a dramatic increase in the LSPR-induced local field was observed in the case of ZnSe quantum dot standing in isolation over the Ag NPs in comparison with that of the ZnO/TiO_2/ZnSe/Ag NWs (Fig. 6(d)). In this sense, Ag NP-embedded structures are beneficial in enhancing the LSPR effect and light absorption. The superior optical performance of ZnO/TiO_2/Ag/ZnSe NWs will facilitate their application in photocatalytic activities.

Photocatalytic degradation was performed on the two types of coaxial NWs under UV and visible light irradiation. Figs. 7(a-d) show the Raman spectra as a function of the irradiation time from 0 min to 120 min. The intensities of the Raman signals of the samples declined as the irradiation time increased, thereby demonstrating efficient degradation. The degradation ratio

curves under UV and visible light irradiation are plotted in Figs. 7(e) and (f), respectively, for further analysis and comparison. The degradation rate under UV light irradiation was faster than that under visible light irradiation. Moreover, almost all of R6G had been decomposed after UV light irradiation for 120 min. This phenomenon was due to the stronger UV light absorption compared with the visible light absorption. More importantly, the ZnO/TiO_2/Ag/ZnSe NWs exhibited higher photocatalytic activity under both visible and UV light irradiation compared with the ZnO/TiO_2/ZnSe/Ag NWs.

To explain the aforementioned photocatalytic activities, possible mechanisms for different structures were proposed on the basis of electron transfer models combined with band structure alignment. As shown in Fig. 8(a), the electrons of TiO_2 and ZnSe in the valence band (VB) of the ZnO/TiO_2/ZnSe/Ag NWs were excited to their conduction band (CB) under UV light irradiation, thus leaving holes in the VB. Photo-generated electron-hole pairs were then efficiently separated at the interface because of the type II band alignment at the TiO_2/ZnSe interface, which resulted in the electron accumulation in TiO_2 and hole accumulation in ZnSe. Meanwhile, the intrinsic electric field in the interface of the Ag/ZnSe Schottky junction could force the transfer of some photo-generated electrons in the ZnSe NPs to the Ag NPs. At this time, the holes in the ZnSe layer would easily react with H_2O in air to produce hydroxyl radicals (·OH). By contrast, the electrons in the Ag NPs would react with adsorbed O_2 to form superoxide radical ($\cdot O_2^-$). The generated

reactive oxygen species (·OH and $\cdot O_2^-$) have a high level of oxidative activity, which could effectively degrade the adsorbed R6G molecules [37]. The electrons in the VB of ZnSe were excited to the CB under visible light irradiation, thereby generating electron-hole pairs. Moreover, hot electrons could be yielded in the Ag NPs because of the LSPR effect and then injected into the CB of ZnSe. The accumulated electrons and holes on the surface could also be captured by O_2 and H_2O to yield $\cdot O_2^-$ and ·OH, respectively, which consequently degraded R6G molecules. This process provides a clear explanation for the enhanced photocatalytic performance in the UV and visible light range caused by the effective charge [38, 39]. Figs. 8(b-d) display the photocatalytic mechanisms of the ZnO/TiO_2/Ag/ZnSe NWs, which correspond to the three types of structures indicated in Fig. 5. In the case of the Ag NPs fully covered by the ZnSe layer (Fig. 8(b)), only the outermost ZnSe layer participated in the degradation reaction of the R6G molecules, resulting in the wasting of accumulated electrons in the TiO_2 layer. Obviously, this structure is not conducive to high-efficiency degradation. However, the NWs with partial coverage of the Ag NPs (Figs. 8(c) and (d)) showed that not only all materials but also all photo-generated electrons or holes participated in the degradation process. Moreover, they had stronger light absorption compared with the ZnO/TiO_2/ZnSe/Ag NWs (Fig. 6(a)). Hence, the two types of structures contributed to the enhanced degradation efficiency illustrated in Figs. 7(e) and (f). Notably, the structure with ZnSe quantum dots standing in isolation over

the Ag NP featured a larger surface area and stronger LSPR effect (Fig. 6(d)) compared with the other structure. This result indicates that the aforementioned structure is the most preferable structure for photocatalytic applications.

4. Conclusions

In summary, we explored the dependence of photocatalytic performance on structures in multi-shell NWs consisting of semiconductor sensitizers and noble metal nanoparticles (NPs). The morphological and structural studies via SEM, XRD, and TEM analyses demonstrated the successful fabrication of ZnO/TiO_2/ZnSe/Ag(NPs) and ZnO/TiO_2/Ag(NPs)/ZnSe coaxial NWs. Three types of surface structures formed by the combination of Ag NPs and ZnSe shell layers were observed in the ZnO/TiO_2/Ag(NPs)/ZnSe NWs. The UV-vis absorption spectral studies illustrated that the light absorption performance of the NWs varied with the compositions and structures of the NWs and that the strongest absorption occurred in the ZnO/TiO_2/Ag(NPs)/ZnSe NWs. The FDTD simulations revealed that the Ag NPs could induce a strong LSPR effect in the embedded structures (corresponding to the ZnO/TiO_2/Ag(NPs)/ZnSe NWs), which contributed to the improved light absorption. Consequently, considerably enhanced photocatalytic degradation of R6G molecules was observed in the UV and visible light regions in the ZnO/TiO_2/Ag(NPs)/ZnSe

NWs. Finally, an optimal structure, that is, multi-shell NWs with ZnSe quantum dots standing in isolation over Ag NPs, was proposed on the basis of the analysis of photocatalytic mechanisms. This study provides guidance to the design of composite materials with noble metal NPs decoration for high-efficiency photocatalytic applications.

Acknowledgements

The work was supported by the "973" Program (2012CB619301), the National Natural Science Foundation of China (61227009), the Natural Science Foundation of Fujian Province of China (2015J01028), and the Fundamental Research Funds for the Central Universities (20720150027，20720160044 and 20720150033).

References

1 M. N. Chong, B. Jin, C. W. K. Chow and C. Saint, *Water Research*, 2010, 44, 2997-3027.

2 C. C. Wang, J. R. Li, X. L. Lv, Y. Q. Zhang and G. S. Guo, *Energy Environ. Sci.*, 2014, **7**, 2831-2867.

3 J. C. Zhao, C. C. Chen and W. H. Ma, *Topics in Catalysis*,2005, **35**, 269-278.

4 X. B. Chen, L. Liu, Y. Yu and S. Mao, *Science*, 2011, **331**, 746-749.

5 A. Fujishima, X. T. Zhang and D. A. Tryk, *Surf. Sci. Rep.*, 2008, **63**, 515-582.

6 H. Yamashita, Y. Ichihashi, M. Takeuchi, S. Kishiguchi and M. Anpo, *J. Synchrotron Radiat.*, 1999, **6**, 451-452.

7 M. Anpo, Y. Ichihash, M. Takeuchi and H. Yamashita, *Res. Chem lntermed*, 1998, **24**, 1443-149.

8 R. Asahi, T. Morikawa, T. Ohwaki, K. Aoki and Y. Taga, *science*, 2001, **293**, 269-271.

9 J. F. Zhu, Z. G. Deng, F. Chen, J. L. Zhang, H. J. Chen, M. Anpo, J. Z. Huang and L. Z. Zhang, *Appl. Catal. B: Environmental*, 2006, **62**, 329-335.

10 Y. Xu, Y. P. Mo, J. Tian, P. Wang, H. G. Yu and J. G. Yu, *Appl. Catal. B: Environmental*, 2016, **181**, 810-817.

11 R. zhou, Q. F. Zhang, E. Uchaker, L. Yang, N.Q. Yin, Y. H. Chen, M. Yin, and G. Z. Cao, *Electrochim. Acta*, 2014, **135**, 284-292.

12 Z. M. Wu, Y. Zhang, J. J. Zheng, X. G. Lin, X. H. Chen, B. W. Huang, H. Q. Wang, K. Huang, S. P. Li and J. Y. Kang, *J. Mater. Chem.*, 2011, **21**, 6020.

13 P. Wang, D. Z. Li, J. Chen, X. Y. Zhang, J. Xian, X. Yang, X. Z. Zheng, X. F. Li and Y. Shao, *Appl. Catal. B: Environmental*, 2014, **160-161**, 217-226.

14 Q. H. Chen, Y. J. Xin and X. W. Zhu, *Electrochim. Acta,* 2015, **186**, 34-42.

15 S. G. Kumar, and L. G. Devi, *J. Phys. Chem. A*, 2011, **115**, 13211-13241.

16 H. Fang, C. X. Zhang, L. Liu, Y. M. Zhao and H. J. Xu, *Biosens. Bioelectronics*, 2015, **64**, 434-441.

17 J. Lu, H. H. Wang, S. J. Dong, F. Q. Wang and Y. F. Dong, *J. Alloy. Compd.*, 2014, **617**, 869-876.

18 S. Li, Q. Tao, D. W. Li, K. Liu and Q. Y. Zhang, *J. Mater. Res.*, 2014, **30**, 304-314.

19 K. Awazu, M. Fujimaki, C. Rockstuhl, J. Tominaga, H. Murakami, Y. Ohki, N. Yoshida and T. Watanabe, *J. Am. Chem. Soc.*, 2008, **130**, 1676-1680.

20 S. T. Ren, G. L. Zhao, Y. Y. Wang, B. Y. Wang and Q. Wang, *Nanotechnology*, 2015, **26**, 125403.

21 X. L. Zhang, Y. Li, J. L. Zhao, S. G. Wang, Y. D. Li, H. T. Dai and X. W. Sun, *J. Power Sources*, 2014, **269**, 466-472.

22 D. C. Hurum, A. G. Agrios, K. A. Gray, T. Rajh and M. C. Thurnauer, *J. Phys. Chem. B*, 2003, **107**, 4545-4549.

23 L. G. Bettini, M. V. Dozzi, F. D. Foglia, G. L. Chiarello, E. Selli, C. Lenardi, P. Piseri and P. Milani, *Appl. Catal. B: Environmental*, 2015, **178**, 226-232.

24 J. Dai, J. Yang, X. H. Wang, L. Zhang and Y. J. Li, *Appl. Surf. Sci.*, 2015, **349**, 343-352.

25 H. Li, X. J. Shen, Y. D. Liu, L. Z. Wang, J. Y. Lei and J. L. Zhang, *J. Alloy. Compd.*, 2015, **646**, 380-386.

26 H. L. Hou, M. H. Shang, L. Wang, W. Li, B. Tang and W. Y. Yang, *Scientific Rep.*, 2015, **5**, 15228.

27 I. N. Martyanov, S. Uma, S. Rodrigues and K. J. Klabunde, *Chem. Commun.*, 2004, **21**, 2476-2477.

28 J. D. Zhuang, W. X. Dai, Q. F. Tian, Z. H. Li, L. Y. Xie, J. X. Wang, P. Liu, X. C. Shi and D. H. Wang, *Langmuir*, 2010, **26**, 9686-9694.

29 X. Y. Pan, M. Q. Yang, X. Z. Fu, N. Zhang and Y. J. Xu, *Nanoscale*, 2013, **5**, 3601-3614.

30 M. K. Nowotny, L. R. Sheppard, T. Bak, and J. Nowotny, *J. Phys. Chem.*, 2008, **112**, 5275-5300.

31 Y. S. Zang, J. Yin, X. He, C. Yue, Z. M. Wu, J. Li and J. Y. Kang, *J. Mater. Chem. A*, 2014, **2**, 7747.

32 A.I. Henry, J. M. Bingham, E. Ringe, L. D. Marks, G. C. Schatz and R. P. Van Duyne, *J. Phys. Chem. C*, 2011, **115**, 9291-9305.

33 X. Zhang, Y. L. Chen, R. S. Liu and D. P. Tsai, *Rep. Prog. Phys.*, 2013, **76**, 046401.

34 A. J. Haes, S. l. Zou, J.Zhao, G. C. Schatz, and R. P. V.Duyne, *J. Am. Chem. Soc.*, 2006, **128**, 10905-10914.

35 C. V. Gopi, M. Venkata-Haritha, S. K. Kim and H. J. Kim, *Nanoscale*, 2015, **7**, 12552-12563.

36 S. Cho, J. W. Jang, J. Kim, J. S. Lee, W. Choi, and K. H. Lee, *Langmuir*, 2011, **27**, 10243-10250.

37 T. H. Yang, L. D. Huang, Y. W. Harn, C. C. Lin, J. K. Chang,C. I. Wu and J. M. Wu, *Small*, 2013, **9**, 3169.

38 Z. Zhang and J. T. Yates, Jr, *Chem. Rev.*, 2012, **112**, 5520-5551.

39 J. Tian, Z. H. Zhao, A. Kumar, R. I. Boughton and H. Liu, *Chem. Soc. Rev.*, 2014, **43**, 6920-6937.

Figure Captions

Fig. 1 Schematic of the formation of multi-shell coaxial NWs. (a) ZnO/TiO_2/ZnSe/Ag and (b) ZnO/TiO_2/Ag/ZnSe.

Fig. 2 SEM images of different NW samples. (a) Bare ZnO NWs; (b) annealed ZnO/TiO_2/Ag NWs; (c) annealed ZnO/TiO_2/ZnSe/Ag NWs; and (d) annealed ZnO/TiO_2/Ag/ZnSe NWs.

Fig. 3 X-ray diffraction patterns of ZnO NWs and different composite coaxial NWs.

Fig. 4 (a) Low-magnification TEM image of ZnO/TiO_2/ZnSe/Ag coaxial NW; (b) EDS line-scan profile of Zn, Se, O, Ti, Ag; (c) HRTEM image of ZnO/TiO_2/ZnSe/Ag coaxial NW.

Fig. 5 (a) Low-magnification TEM image of ZnO/TiO_2/Ag/ZnSe coaxial NW; (b) EDS line-scan profile of Zn, Se, O, Ti, Ag; (c) and (d) HRTEM image of ZnO/TiO_2/Ag/ZnSe coaxial NW.

Fig. 6 (a) UV-visible absorption spectra of ZnO/TiO_2/ZnSe/Ag, ZnO/TiO_2/Ag/ZnSe NWs, and intermediate samples. Simulated near-field distributions of (b) ZnO/TiO_2/ZnSe/Ag NW; (c) ZnO/TiO_2/Ag/ZnSe NW with the Ag NP fully covered by the outside ZnSe layer; (d) ZnO/TiO_2/Ag/ZnSe NW with the ZnSe quantum dot standing in isolation over the Ag NP. The intensity is on a log scale.

Fig. 7 Raman spectra of R6G (10^{-5} M) treated with UV and visible light irradiation on (a-b) ZnO/TiO_2/ZnSe/Ag NWs and (c-d) ZnO/TiO_2/Ag/ZnSe NWs. The degradation ratio (I/I_0) curves for R6G under (e) UV and (f) visible light

irradiation. I_0 and I represent the Raman signal intensity at approximately 611 cm^{-1} without and with light irradiation for a certain time, respectively.

Fig. 8 Energy bandgap and photocatalytic mechanisms of different nanostructures under UV and visible light irradiation. (a) ZnO/TiO_2/ZnSe/Ag NWs; (b) ZnO/TiO_2/Ag/ZnSe NWs with the Ag NPs fully covered by the outside ZnSe layer; (c) ZnO/TiO_2/Ag/ZnSe NWs with the Ag NPs partially covered by the ZnSe layer, which is in contact with the TiO_2 layer; (d) ZnO/TiO_2/Ag/ZnSe NWs with the ZnSe quantum dots standing in isolation over the Ag NPs.

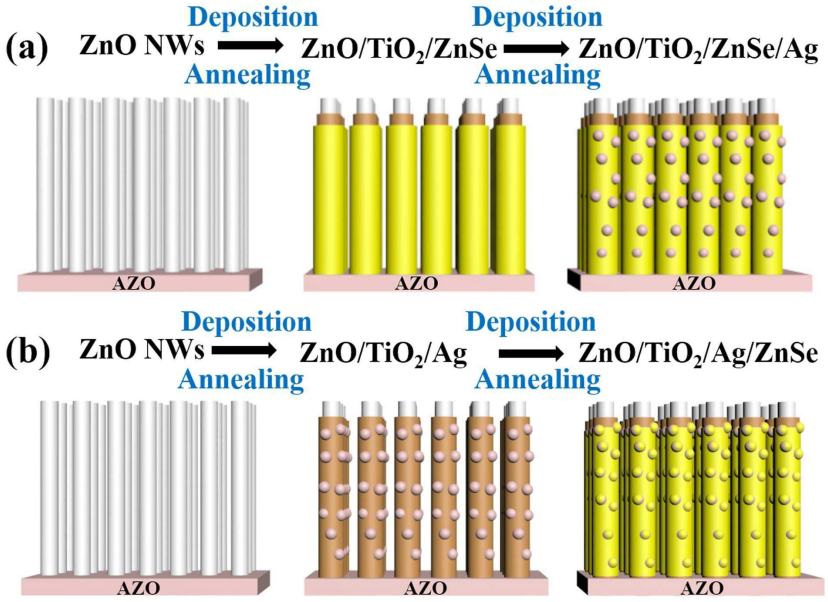

Figure 1 Schematic of the formation of multi-shell coaxial NWs.

(a) $ZnO/TiO_2/ZnSe/Ag$ and (b) $ZnO/TiO_2/Ag/ZnSe$.

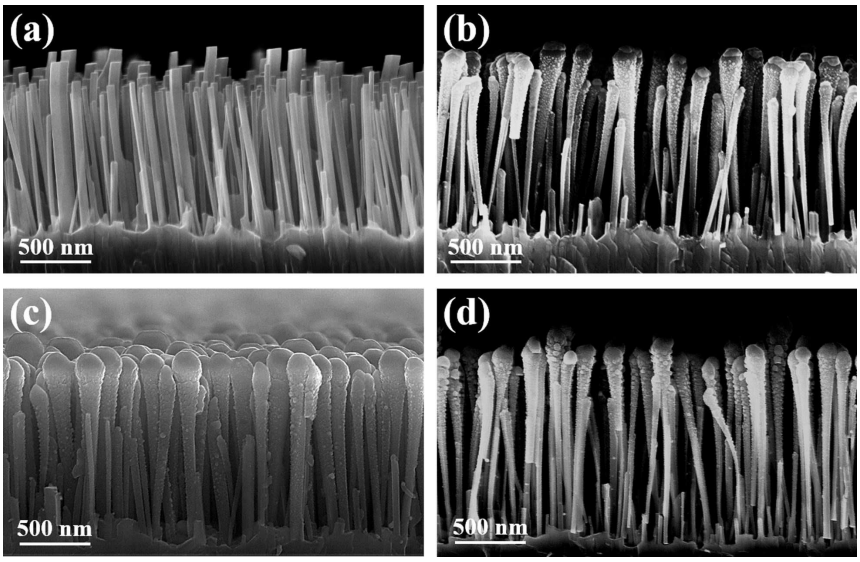

Figure 2 SEM images of different NW samples. (a) Bare ZnO NWs; (b) annealed ZnO/TiO_2/Ag NWs; (c) annealed ZnO/TiO_2/ZnSe/Ag NWs; and (d) annealed ZnO/TiO_2/Ag/ZnSe NWs.

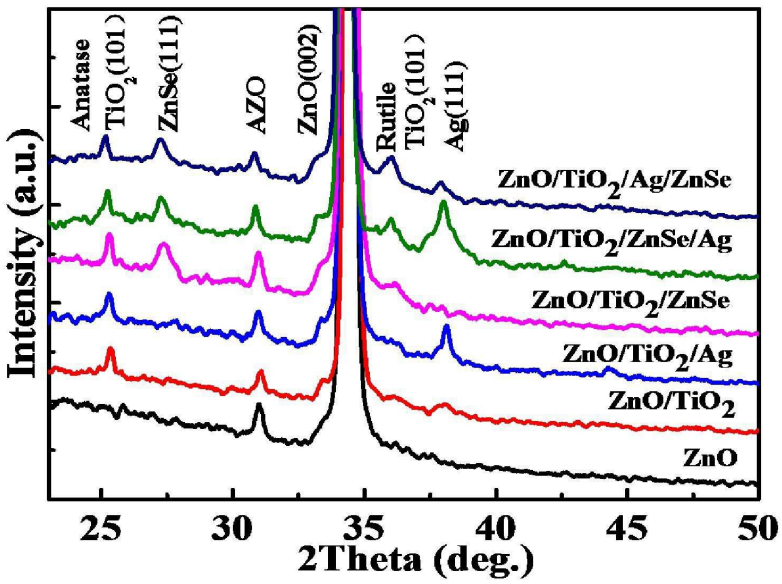

Figure 3 X-ray diffraction patterns of ZnO NWs and different composite coaxial NWs.

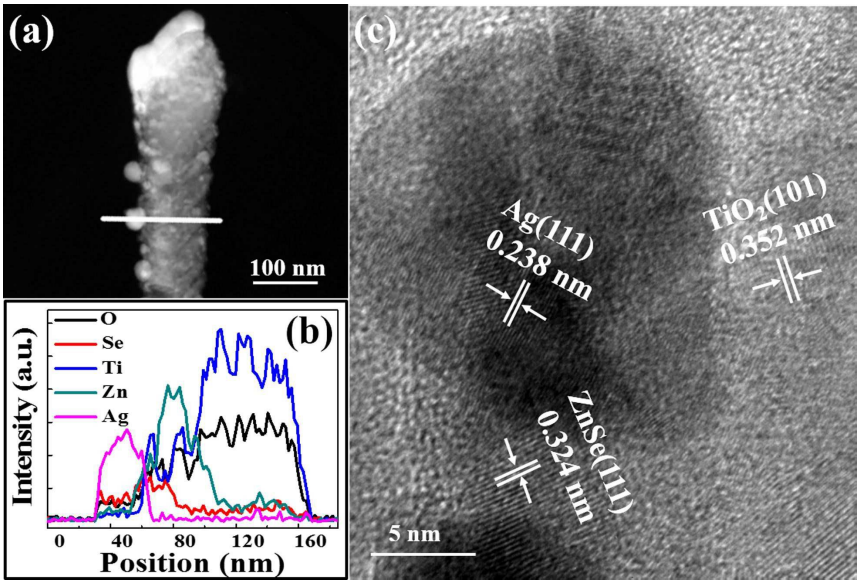

Figure 4 (a) Low-magnification TEM image of ZnO/TiO_2/ZnSe/Ag coaxial NW; (b) EDS line-scan profile of Zn, Se, O, Ti, Ag; (c) HRTEM image of ZnO/TiO_2/ZnSe/Ag coaxial NW.

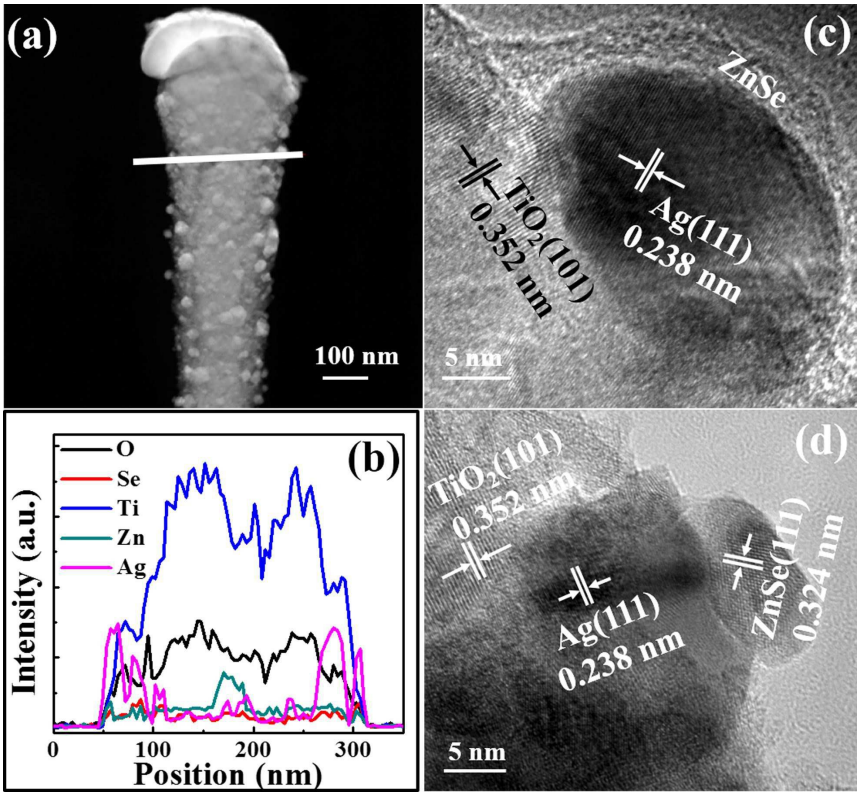

Figure 5 (a) Low-magnification TEM image of ZnO/TiO_2/Ag/ZnSe coaxial NW; (b) EDS line-scan profile of Zn, Se, O, Ti, Ag; (c) and (d) HRTEM image of ZnO/TiO_2/Ag/ZnSe coaxial NW.

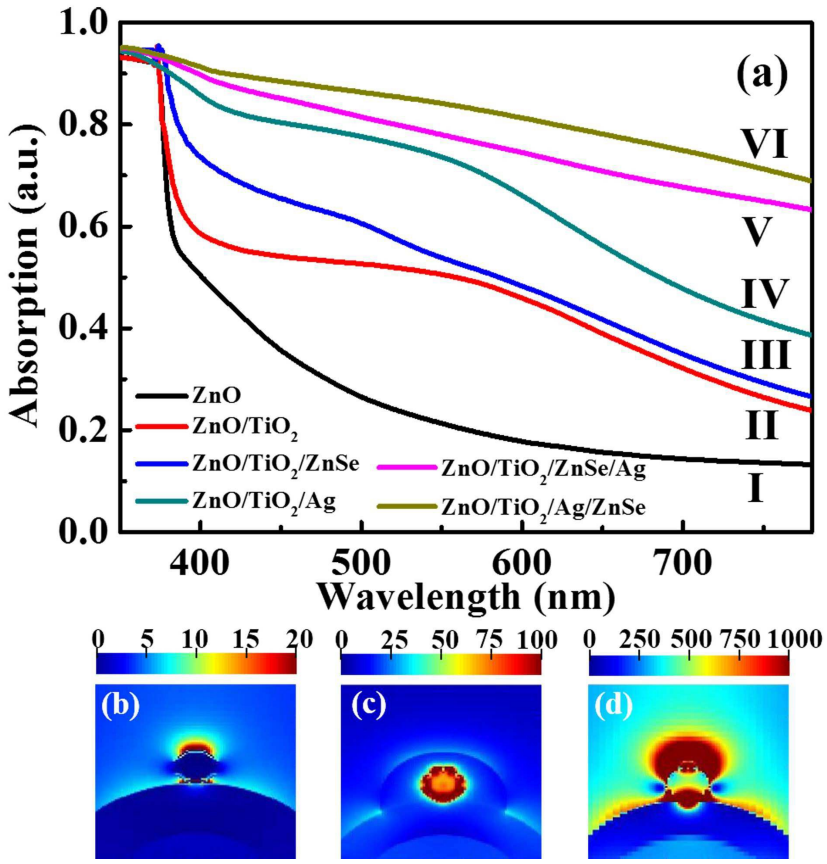

Figure 6 (a) UV-visible absorption spectra of ZnO/TiO2/ZnSe/Ag, ZnO/TiO2/Ag/ZnSe NWs, and intermediate samples. Simulated near-field distributions of (b) ZnO/TiO2/ZnSe/Ag NW; (c) ZnO/TiO2/Ag/ZnSe NW with the Ag NP fully covered by the outside ZnSe layer; (d) ZnO/TiO2/Ag/ZnSe NW with the ZnSe quantum dot standing in isolation over the Ag NP. The intensity is on a log scale.

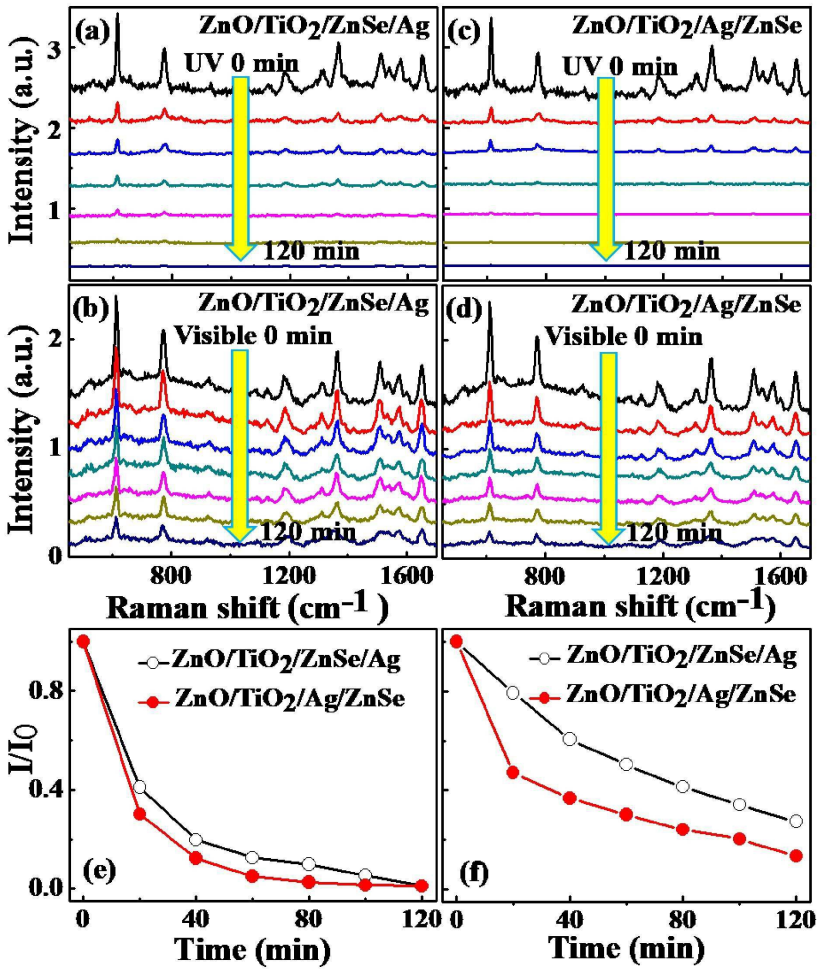

Figure 7 Raman spectra of R6G (10^{-5} M) treated with UV and visible light irradiation on (a-b) $ZnO/TiO_2/ZnSe/Ag$ NWs and (c-d) $ZnO/TiO_2/Ag/ZnSe$ NWs. The degradation ratio (I/I_0) curves for R6G under (e) UV and (f) visible light irradiation. I_0 and I represent the Raman signal intensity at approximately 611 cm^{-1} without and with light irradiation for a certain time, respectively.

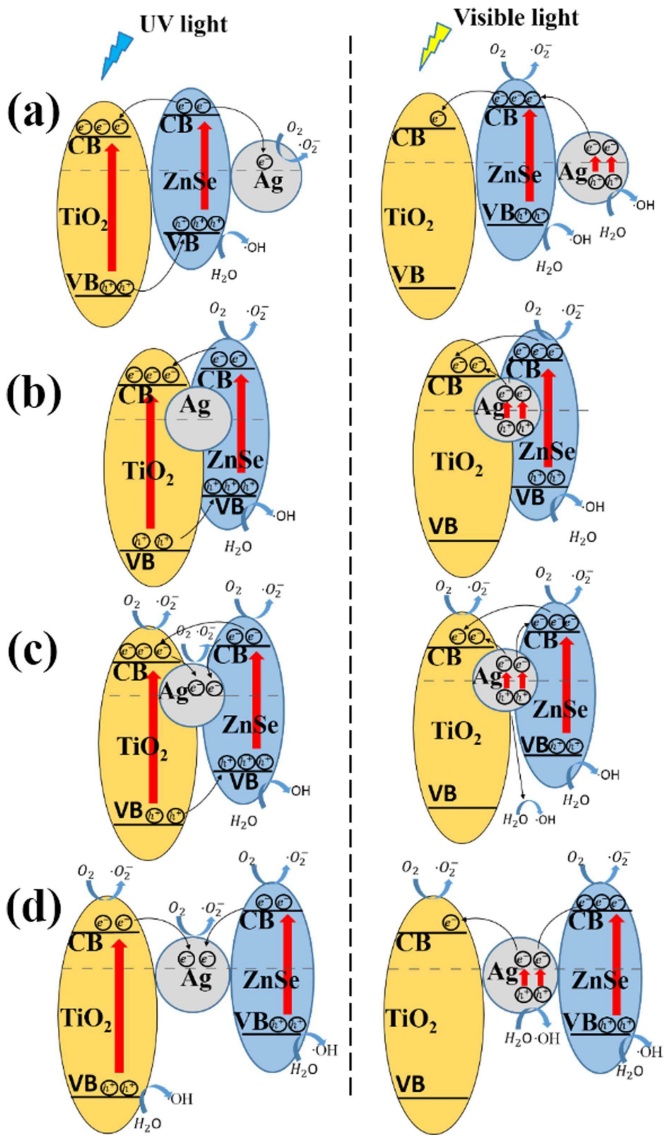

Figure 8 Energy bandgap and photocatalytic mechanisms of different nanostructures under UV and visible light irradiation. (a) ZnO/TiO_2/ZnSe/Ag NWs; (b) ZnO/TiO_2/Ag/ZnSe NWs with the Ag NPs fully covered by the outside ZnSe layer; (c) ZnO/TiO_2/Ag/ZnSe NWs with the Ag NPs partially covered by the ZnSe layer, which is in contact with the TiO_2 layer; (d) ZnO/TiO_2/Ag/ZnSe NWs with the ZnSe quantum dots standing in isolation over the Ag NPs.

Graphical abstract

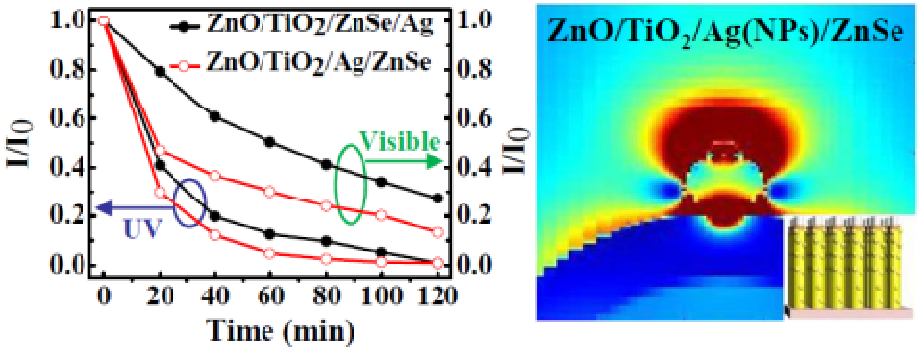

The photocatalytic activity of $ZnO/TiO_2/Ag/ZnSe$ nanowires was significantly enhanced under light irradiation compared with that of $ZnO/TiO_2/ZnSe/Ag$ nanowires.